JOURNAL OF MATERIALS SCIENCE 25 (1990) 35–44

Elevated temperature slow plastic deformation of NiAl–TiB_2 particulate composites at 1200 and 1300 K

J. DANIEL WHITTENBERGER
NASA-Lewis Research Center Cleveland, Ohio 44135, USA
R. K. VISWANADHAM*, S. K. MANNAN, B. SPRISSLER
Martin Marietta Laboratories, 1450 South Rolling Rd., Baltimore, Maryland 21227-3898, USA

Elevated temperature compression testing has been conducted in air at 1200 and 1300 K with strain rates varying from $\sim 10^{-4}$ to $\sim 10^{-7}$ sec^{-1} on NiAl–TiB_2 particulate composites. These materials, which consisted of a B2 crystal structure intermetallic Ni–50 at % Al matrix and from 0 to 30 vol % of approximately 1 μm diameter TiB_2 particles, were fabricated by XD synthesis and hot pressed to full density. Flow strength of the composites increased with volume fraction of the strengthening phase with NiAl–30TiB_2 being approximately three times stronger than NiAl. Comparison of the light optical and transmission electron microstructures of as-received and tested samples revealed that reactions did not occur between the two phases, and NiAl–TiB_2 interfaces were not cracked during deformation. Additional transmission electron microscopy indicated that the particles stabilize a vastly different microstructure in the NiAl matrix of the composites than that formed in unreinforced NiAl.

1. Introduction

As a class of high temperature materials, intermetallics can serve as the bridge between metals, such as superalloys or refractory metals, and promising structural ceramics, for examples SiC and Si_3N_4. This role is possible since some intermetallics possess sufficient metal-like behaviour that they can be produced and fabricated by "traditional" metallurgical methods, yet they have properties which can not be realized in current alloys. The nominally equiatomic aluminides of cobalt and nickel are examples of such intermetallics. They can be made by melting and casting [1–6] or powder metallurgy techniques [7, 8] and formed into shapes by electrodischarge machining and grinding. Additionally both NiAl and CoAl have very high melting points (greater than 1900 K), relatively low densities (of the order of 6 $Mg\,m^{-3}$), cubic crystal structures and the basic framework for excellent oxidation resistance.

Unfortunately the inherent elevated temperature mechanical strength of these two aluminides, particularly NiAl [8] is lacking. While some degree of strengthening can be achieved by grain refinement [9, 10], under high temperature–slow strain rate conditions grain boundary deformation mechanisms become more important, and the strength of NiAl decreases with a decreasing grain size. Ternary alloying additions which lead to precipitation can also make this aluminide more resistant to deformation [11, 12]; however at elevated temperatures such second-phase particles tend to grow and/or dissolve thus becoming less effective strengtheners.

Dissolution or growth of the strengthening phase can be avoided if it is thermodynamically stable and essentially insoluble in the matrix. While there are many schemes for producing such materials (for example, the incorporation of an element in the alloy which can be selectively oxidized or the addition of a compound that is soluble in the melt but not the solid), Martin Marietta Laboratories is currently developing a solid state method, the XD process, which directly yields discontinuously reinforced metal matrix composites. Under a current programme sponsored by the Office of Naval Research, an attempt [13] is being made to apply this technology to NiAl in an effort to improve the elevated temperature strength and possibly the low temperature fracture toughness.

This paper describes results from the initial attempt to produce intermetallic particulate composites by the XD process. Materials containing from 0 to 30 vol % of nominally 1 μm TiB_2 particles as the strengthening phase in a NiAl matrix have been fabricated, and these were tested in compression at 1200 and 1300 K with strain rates ranging from 10^{-4} to 10^{-7} sec^{-1}. Both light optical and transmission electron microscopy techniques were used to characterize the microstructures of the as received and tested composites.

2. Experimental procedures

The XD process was utilized to produce Ni–50 at %

* *Present address* Multi-Metals 715 E. Gray St., Louisville, Kentucky 40202, USA.

0022–2461/90 $03.00 + .12

Al particulate composites containing from 0 to 30 vol % TiB_2 particles. This phase was chosen to be the strengthening agent because of its high melting point (3063 K), elevated temperature strength [14] and compatibility with aluminides [15]. Additionally its lower density ($\sim 4.5\,Mg\,m^{-3}$) could lead to significant weight savings, especially for high particulate loadings. Following XD synthesis, the materials were compacted to full density by vacuum hot pressing at 28 MPa and 1675 to 1775 K utilizing graphite tooling.

Right cylindrical compression specimens 12 mm long with a 5.5 mm diameter were prepared by electrodischarge machining and grinding where their length was parallel to the hot pressing direction. Constant velocity compression tests at speeds ranging from 2.12×10^{-3} to $2.12 \times 10^{-6}\,mm\,sec^{-1}$ were conducted in a universal test machine to $\sim 10\%$ strain at 1200 and 1300 K in air. The autographically recorded load–time charts were converted to true compressive stresses, strains, and strain rates via the offset method and the assumption of conservation of volume. Additional details regarding the test procedures can be found in [7] and [16].

Both light optical and transmission electron microscopy (TEM) techniques were used to characterize the structure of selected as received and compression tested samples. Grain sizes were determined by the circle intercept method after the microstructures had been revealed by immersion etching in a mixed acid solution (33 parts by volume of acetic, HCl and HNO_3 acids plus 1 part HF). Sections taken perpendicular to the hot pressing (compression) axis by cutting slices approximately 0.5 mm thick with a high speed diamond saw were used for TEM examination. These were ground on resin-bonded diamond wheels to a thickness of ~ 0.2 mm, adhesively mounted between glass slides and 3 mm diameter circular discs cut by ultrasonic grinding in a SiC slurry. The discs were electrolytically thinned to perforation with a 10% perchloric–methanol solution at 238 K and 10 to 12 V.

3. Results

3.1. Materials

NiAl-based particulate composites containing 0, 2.5, 5, 7.5, 10, 20 and 30 vol % TiB_2 were produced, and examination of the hot pressed materials revealed that all compositions were fully dense, as little sign of porosity or cracking could be found. Typical light optical photomicrographs of as fabricated composites are given in Fig. 1. The TiB_2 particles, appearing as the light gray phase in these photographs, tended to be evenly dispersed in the low volume fraction materials (Fig. 1a) but not at the higher loadings (Fig. 1b). Due to the powder-based processing approach, the composites also contained a lower volume fraction of Al_2O_3 particles (black phase in Fig. 1) in addition to the TiB_2. While the alumina resided principally on the grain boundaries, the titanium diboride was distributed both within the grains and along boundaries (Fig. 1a).

Because of the non-uniformity of TiB_2 particle distribution, grain sizes for the 20 and 30 vol % composites could not realistically be determined; however they, as typified by Fig. 1a, were measurable for the low volume fractions, and the average grain diameter data are given in Table I. In general the grain structures were somewhat elongated perpendicular to the hot pressing direction, and this tendency toward pancake shaped grains increased as the TiB_2 content increased.

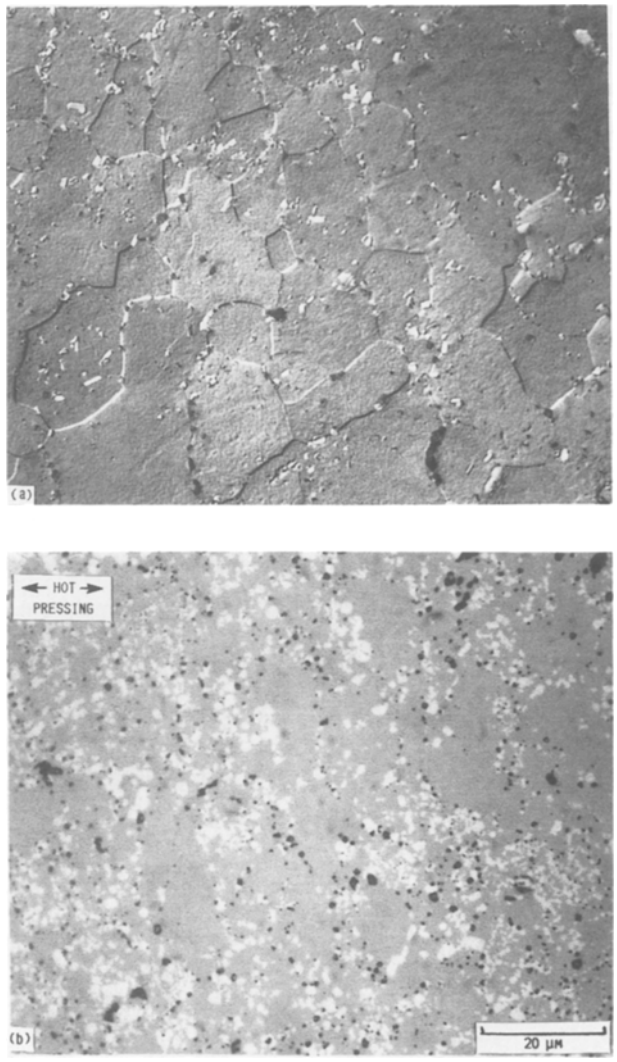

Figure 1 Light optical photomicrographs of as-fabricated NiAl–TiB_2 materials. (a) etched, 2.5 vol %, differential interference contrast (DIC), (b) unetched, 20 vol %.

TEM studies of the as-fabricated composites demonstrated that the low volume fraction materials appeared to be relatively dislocation-free (Fig. 2a) while the higher particulate loadings (Fig. 2b) exhibited both subgrains and a high density of dislocations in NiAl as well as touching TiB_2 particles. The absence of dislocation activity in the matrix of particle deficient composites (Fig. 2a) is somewhat surprising in view of the processing (hot pressing) to achieve densification and the differences* in thermal expansion between the NiAl matrix and TiB_2 (grey particles) or Al_2O (dark phase). While some titanium diboride particles contained defects in the form of small angle boundaries, stacking faults, dislocation loops and random networks, most TiB_2 particles were devoid of structure. No reaction zone between the titanium diboride particles and NiAl matrix could be seen; however

*At 1300 K the average thermal expansions of NiAl, TiB_2 and Al_2O_3 are 0.0153 [17], 0.0077 [18] and 0.0085 [18] respectively.

TABLE I Summary of grain size data for NiA–TiB_2 composites

Grain Diameter (μm)						
Vol. Fraction TiB_2 %	As-Fabricated		Tested – Longitudinal			
	Cross Section	Longitudinal Section	1200 K		1300 K	
			Approximate Strain Rate, (sec^{-1})			
			2×10^{-5}	2×10^{-7}	2×10^{-5}	2×10^{-7}
0	–	–	13	13	12	11
2.5	13	12	–	–	11	11
5	–	–	–	8	7	8
7.5	11	8	–	8	8	10
10	–	–	8	9	8	9
20	Could not be determined					
30	Could not be determined					

interfacial dislocations at the particle–matrix interface were quite evident (Fig. 2a). In a few foils taken from the high volume fraction composites, additional dislocation loops were observed surrounding some of the TiB_2 particles, but this behaviour was not universal. (Fig. 2b).

3.2. Mechanical Properties

Typical true stress–strain curves for the NiAl–TiB_2 composites as functions of strain rate and temperature are presented in Figs 3 and 4. These illustrate the two general types of behaviour found in the present composites. For materials containing less than 10 vol % of the strengthening phase, deformation under all test conditions occurred at a constant flow stress after a small amount of work hardening (Fig. 3). The 20 and 30 vol % composites, on the other hand, displayed diffuse yielding followed by strain softening (Fig. 4) irrespective of the temperature or strain rate. Behaviour of the 10 vol % material was halfway between these two modes in that diffuse yielding was followed by continued deformation at a slightly reduced but more or less constant stress. The transition from steady state flow to diffuse yielding can be seen in Fig. 5 which presents true compressive stress–strain diagrams as a function of TiB_2 loading for similar deformation conditions.

As is clearly demonstrated in Fig. 5, composite strength increases with particulate loading. This is also evident in Fig. 6 where true compressive stress–strain rate data are presented for both test temperatures. The flow stresses σ and strain rates $\dot{\varepsilon}$ were determined from the separate stress–strain diagrams where σ and $\dot{\varepsilon}$ are average values from constant flow regimes (0, 2.5, 5 and 7.5 vol % materials) or means calculated over the diffuse yield points for the higher volume fraction composites. An alternative, but equally valid view, is that σ represents the flow stress at yielding or about 1% plastic strain.

The stress–strain rate data in Fig. 6 were fitted to the standard power law and temperature compensated power law rate expressions

$$\dot{\varepsilon} = A\sigma^n \tag{1}$$

and

$$\dot{\varepsilon} = B\sigma^n \exp(-Q/RT) \tag{2}$$

where A and B are constants, n is the stress exponent, Q the activation energy for creep, R the gas constant and T the absolute temperature. Fits were accomplished by linear regression techniques, and the results of these calculations including the coefficients of determination R_d^2 are given in Table II. These data show that the stress exponent and activation energy

TABLE II Power law and temperature compensated-power law fits of true compressive flow stress–strain rate data for NiAl–TiB_2 composites

(a) Power law fits

Vol % TiB_2	Temperature					
	1200 K			1300 K		
	A	n	R_d^2	A	n	R_d^2
0[1]	1.28×10^{-17}	6.74	1.0	3.12×10^{-15}	6.00	.998
0[2]	–	–	–	2.34×10^{-16}	6.46	.999
0[3]	–	–	–	3.89×10^{-15}	5.90	.998
2.5	–	–	–	1.46×10^{-19}	8.13	.997
5.0	–	–	–	9.27×10^{-25}	10.67	.988
7.5	2.14×10^{-24}	9.45	.991	8.00×10^{-26}	10.94	.995
10.	3.14×10^{-27}	10.81	.988	2.05×10^{-29}	12.76	.986
20	1.13×10^{-26}	9.63	.998	1.56×10^{-22}	8.30	.990
30	7.14×10^{-29}	10.4	.998	3.03×10^{-21}	7.47	.987
49.9[4,5]	–	–	–	3.43×10^{-15}	6.50	.999
48.3[4,5]	3.93×10^{-15}	5.70	.998	4.30×10^{-14}	5.68	.993

[1]Data from strain rates $\leqslant 2 \times 10^{-5}$ sec^{-1}.
[2]Data from strain rates $> 2 \times 10^{-5}$ sec^{-1}.
[3]All 1300 K data for 0 vol % material.
[4]At % Al
[5][8]

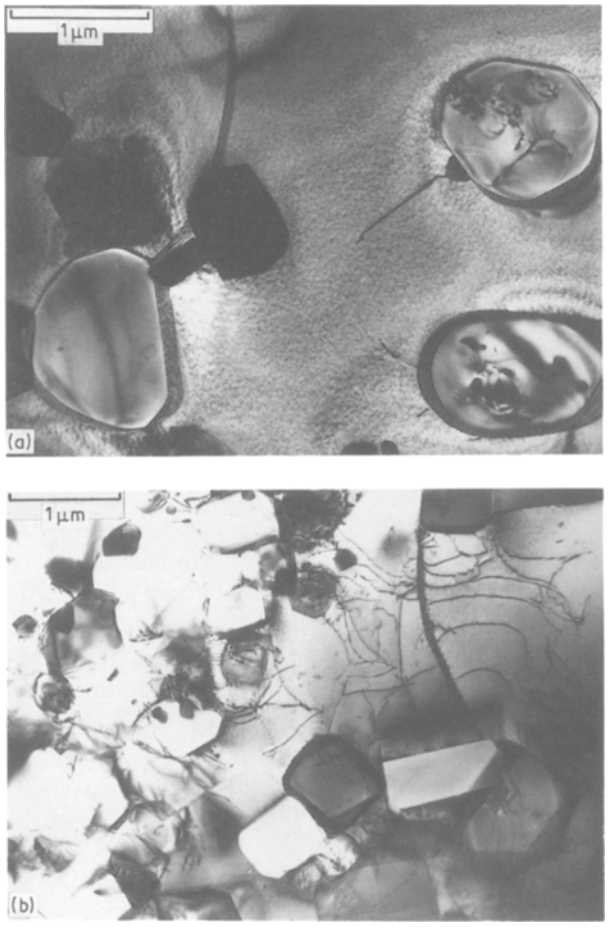

Figure 2 Typical TEM photomicrographs of the microstructure found in as-fabricated NiAl–TiB_2 composites. (a) 5 vol %, (b) 30 vol %.

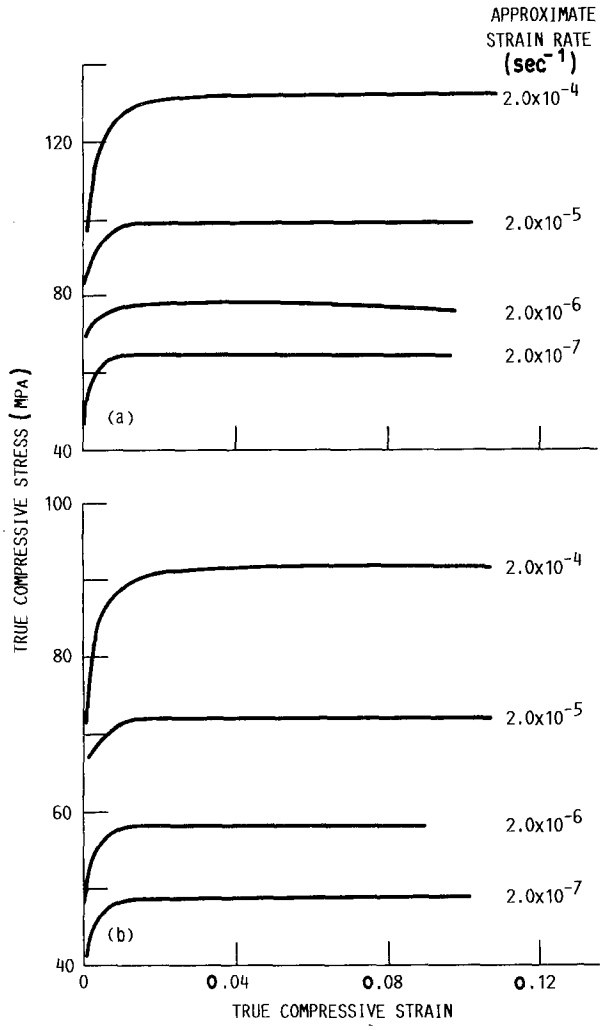

Figure 3 True compressive stress–strain diagrams for NiAl–7.5TiB_2 tested at (a) 1200 K and (b) 1300 K.

for the unstrengthened NiAl are about 6 and 350 kJ mol^{-1} respectively; whereas $8 \leqslant n \leqslant 12$ and $Q \approx 400\,kJ\,mol^{-1}$ for the composites.

As the volume fraction of TiB_2 plays an important role in determining the strength of the composite, the stress–strain rate data were fitted to an equation of the type

$$\dot{\varepsilon} = B\sigma^n v^p \exp(-Q/RT) \quad (3)$$

where v is the volume fraction of TiB_2 particles and p is a constant. Use of all data from the composites yielded

$$\dot{\varepsilon} = 2.96 \times 10^{-11}\sigma^{8.77}v^{-3.27} \exp(-358.9/RT) \quad (4)$$

TABLE II (b) Temperature Compensated-power law fits

Vol % TiB_2	Temperature range (K)	B	n	Q (kJ mol^{-1})	R_d^2
0[1]	1200–1300	0.52	6.33	365.9	.996
0[2]	1200–1300	3.36×10^{-2}	5.94	324.5	.998
5	1200–1300	5.14×10^{-8}	10.3	400.9	.988
7.5	1200–1300	6.85×10^{-8}	10.09	407.6	.988
10	1200–1300	3.14×10^{-10}	11.63	426.8	.980
20	1200–1300	1.07×10^{-7}	8.87	397.5	.989
30	1200–1300	7.28×10^{-6}	7.97	408.6	.973
0[3]	1100–1400	0.16	5.75	314.2	.99

[1]Data from strain rates $\leqslant 2 \times 10^{-5}\,sec^{-1}$.
[2]Data from strain rates $\leqslant 0.2\,sec^{-1}$.
[3][8]

with a 95% coefficient of determination. Although restriction of the data to either (1) the 2.5 to 10 vol % TiB_2 materials or (2) 1300 K testing did somewhat improve the fit (coefficient of determination = 0.97), all analyses based on Equation 3 resulted in p values ranging from -2.75 to -3.25 with values or n and Q similar to those reported in Equation 4.

3.3. Post test microstructure

Light optical examination of longitudinal (parallel to the hot pressing–compression axis) sections of selected specimens indicated that neither grain boundary cracking nor particle–matrix separation occurred. This can be seen in Figs 7 and 8 which illustrate typical microstructures found in NiAl–TiB_2 composites after testing at high temperature–slow deformation (Fig. 7) and lower temperature–faster straining (Fig. 8) conditions. Irrespective of the volume fraction of TiB_2, both the grain and interphase boundaries have remained intact. Additionally measurement of the grain sizes after testing indicated that the as fabricated microstructures were stable since little indication of grain growth was found following testing (Table I).

Inspection of the outer, air exposed surface of test specimens revealed that the Ni–50Al matrix does not impart good oxidation resistance. As shown in Fig. 9 multiphase structures with non-planar interfaces can be formed between the surface oxide and the composite.

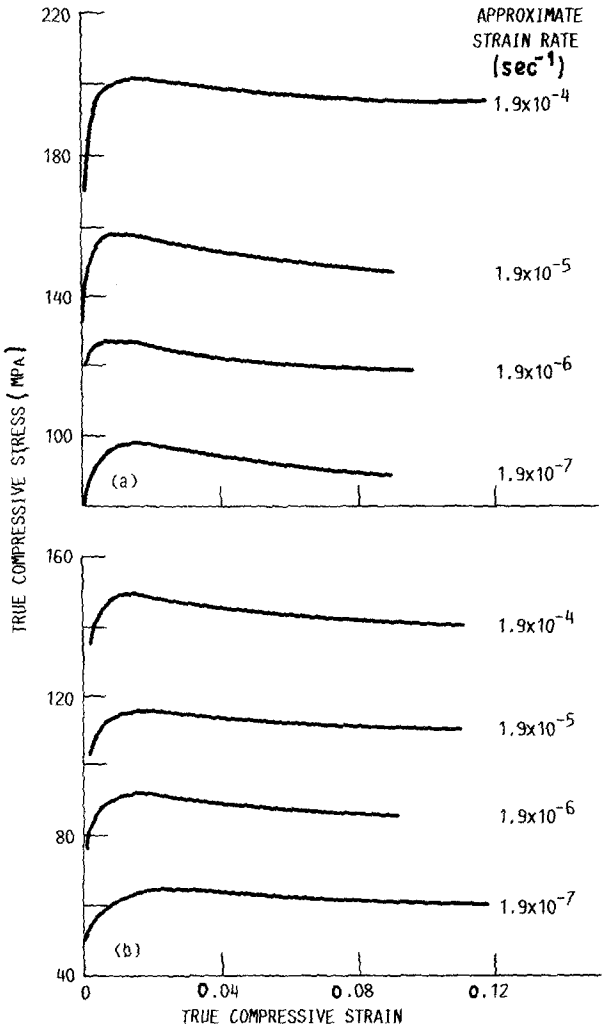

Figure 4 True compressive stress–strain diagrams for NiAl–20TiB_2 tested at (a) 1200 K and (b) 1300 K.

Most probably the intermediate layers visible in Fig. 9a are nickel solid solution (next to the surface oxide) and γ' (between the nickel solid solution and NiAl matrix). Although quantitative methods were not employed, it appears that the TiB_2 is affected by oxidation. Both the number and size of the particles sharply decrease

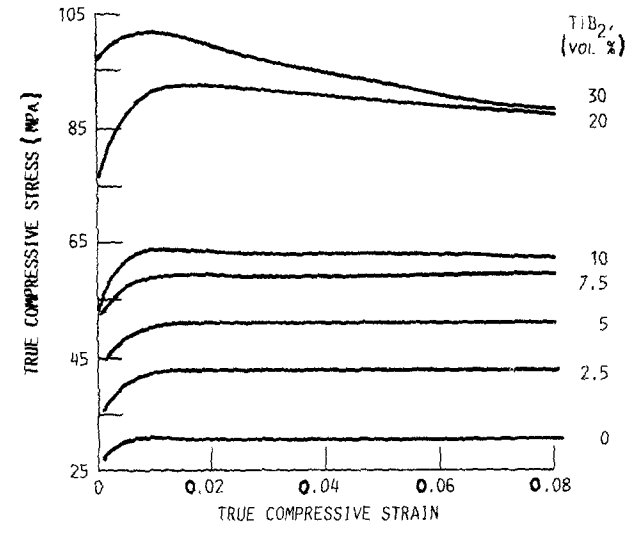

Figure 5 True compressive stress–strain curves for NiAl–TiB_2 composites tested at 1300 K and a strain rate of $\sim 2 \times 10^{-6}$ sec^{-1} as a function of TiB_2 content.

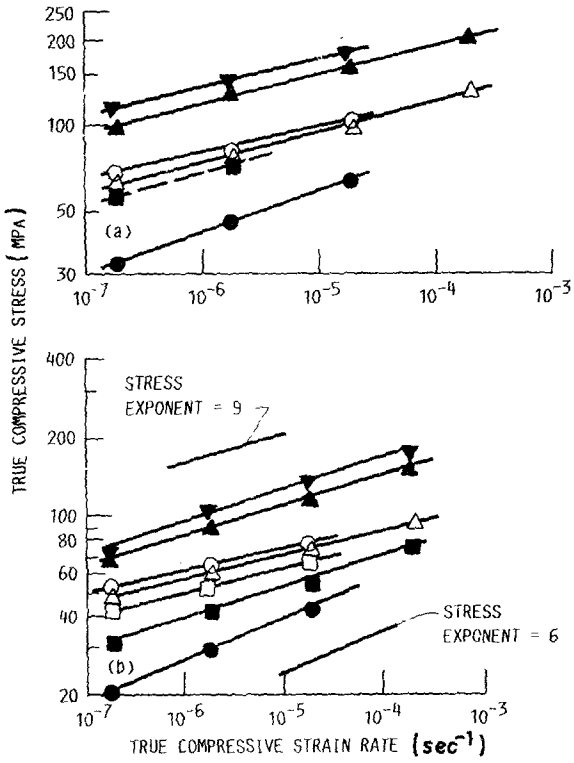

Figure 6 True compressive stress–strain rate plots for NiAl–TiB_2 composites tested at (a) 1200 and (b) 1300 K as a function of TiB_2 content vol %. (● 0, ■ 2.5, □ 5.0, △ 7.5, ○ 10.0, ▲ 20.0, ▼ 30.0).

at the composite–γ' interface (Fig. 9b), and few particles remain as the surface oxide is approached. While the strengthened phase is being affected by oxidization, it is not promoting catastrophic attack of the composite.

Electron microprobe examination of the specimens shown in Fig. 9, as well as NiAl–0TiB_2 samples strained under similar conditions, was conducted. Two traces starting from the surface oxide and running into the bulk material were undertaken on each specimen with aluminium, nickel and titanium characteristic peaks being continuously monitored. The microprobe study confirmed the phase identification, and Table III summarizes the widths of the phase fields obtained both from the microprobe data and measurements from photomicrographs. While relatively sharp boundaries exist between nickel solid solution–γ' and γ'–NiAl, the width of the aluminium-deficient NiAl is somewhat subjective due to the shallowness of the aluminium and nickel concentration gradients as the bulk composition is approached; additionally the width of the aluminium-deficient

TABLE III Summary of microprobe and microstructural measurements on NiAl–TiB_2 composites tested at $\sim 2 \times 10^{-7}$ sec^{-1}

Material	Test temperature (K)	Approximate phase width (μm)					
		Microprobe			Microstructure		
		γ^*	γ'	NiAl[2]	γ^*	γ'	NiAl[2]
NiAl–0TiB_2	1200	–	–	60			
	1300	–	–	110			
NiAl–20TiB_2	1200	4	22	160	4	25	140
	1300	8	40	350	6	35	370

*Nickel solid solution.
[2]Aluminium-deficient NiAl.

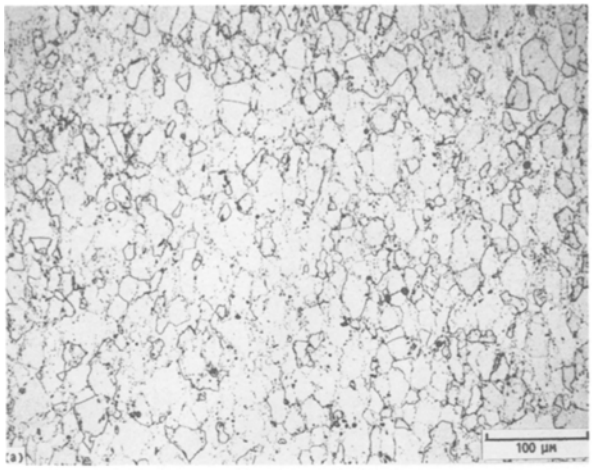

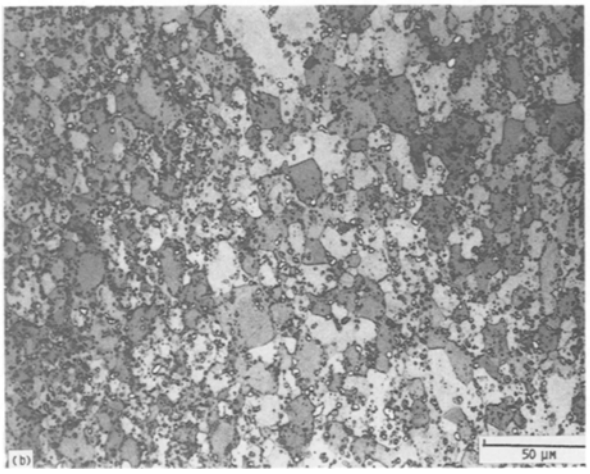

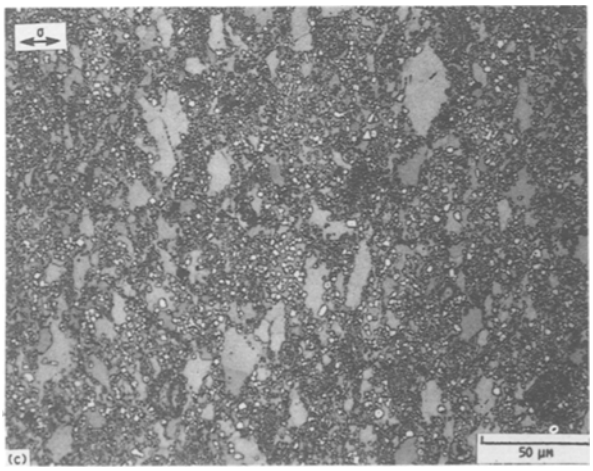

Figure 7 Light optical photomicrographs of the etched microstructure of NiAl–TiB_2 composites after testing at 1300 K and $\dot{\varepsilon} \sim 2 \times 10^{-7}$ sec^{-1}. (a) 0 vol %, tested to 0.094 strain; (b) 5 vol %, tested to 0.098 strain and (c) 30 vol %, tested to 0.105 strain.

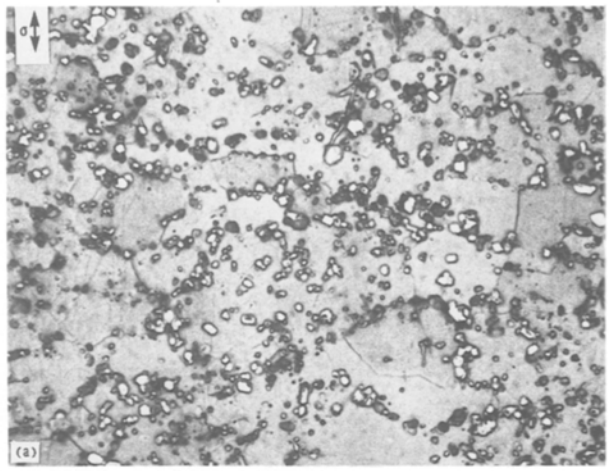

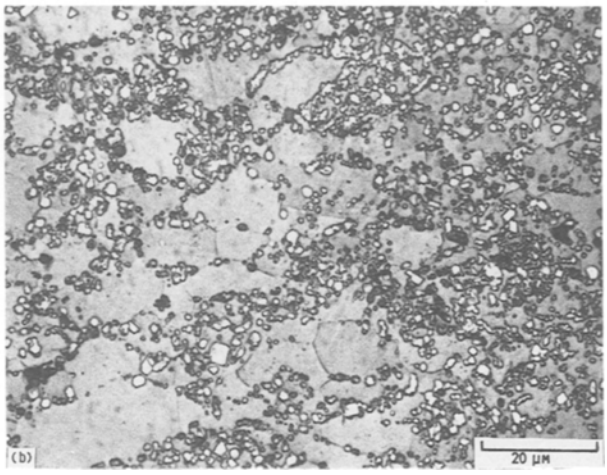

Figure 8 Light optical photomicrographs of the etched microstructure of NiAl–TiB_2 composites after testing at 1200 K and $\dot{\varepsilon} \sim 2 \times 10^{-5}$ sec^{-1}. (a) 7.5 vol %, tested to 0.102 strain and (b) 20 vol %, tested to 0.09 strain.

NiAl for the NiAl–0TiB_2 composites could not be determined from visual examination due to the lack of contrast from etching.

For the TiB_2 containing materials the phase width data (Table III) indicate good agreement between the two techniques; however comparison of the total depth of diffusion (summation of widths of γ, γ' and aluminium-deficient NiAl regions) reveals that there is a 3 + 1-fold difference in widths between the 0 and 20% TiB_2 materials at each test temperature. Additionally examination of the titanium profiles for the TiB_2 containing materials revealed a progressive decrease in the number of titanium-rich particles travelling from the NiAl–γ' interface to the air exposed surface; however the profiles appeared to show that titanium is in solution in both γ' and nickel-rich phase.

Microprobe traces across the oxide layers shown in Figs 9a and b indicated that the air exposed layer consisted of both titanium- and aluminium-rich phases; however attempts to use X-ray diffraction techniques on these particular specimens were unsuccessful due to insufficient material for analysis. The surface oxides formed on NiAl–10TiB_2 deformed under identical conditions (1200 and 1300 K at $\dot{\varepsilon} \sim 2 \times 10^{-7}$ sec^{-1}) could be identified, and they contained Al_2O_3, $NiAl_2O_4$ and TiO_2. While neither samples had evidence of any boron containing phase, the 1200 K tested specimen additionally possessed NiO and $NiTiO_3$ in the scale.

TEM examination of 1300 K tested materials revealed that the TiB_2 profoundly influenced the deformation mechanisms. While well developed, relatively dislocation-free subgrains were formed in the unstrengthened composite (Fig. 10a), the structure (Fig. 10b) of NiAl–10TiB_2 consisted of a high density of tangled dislocation loops in the matrix with subboundaries spanning

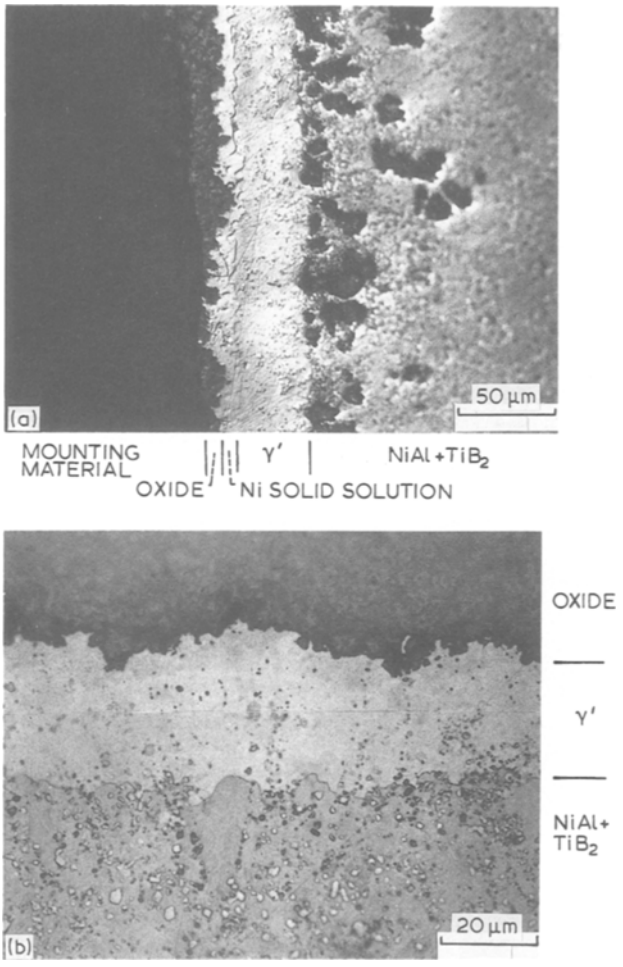

Figure 9 Light optical photomicrographs of the etched microstructure near the surface of NiAl–20TiB_2 composites after testing at $\dot{\varepsilon} \sim 2 \times 10^{-7}\,sec^{-1}$. (a) 1300 K to 0.117 strain [DIC] and (b) 1200 K to 0.09 strain.

adjacent second-phase particles. A gradual transition from only subgrains (Fig. 10a) to the tangled dislocations and subgrains of Fig. 10b occurred as the TiB_2 content was increased in the low volume fraction composites; a typical example of this transition structure is shown in Fig. 10c where subgrains between particles and anchored to high angle grain boundaries can be seen.

Only one high volume fraction specimen was examined by TEM, and the structure (Fig. 10d) is similar to that for the 10 vol % material (Fig. 10b) except the dislocation density in the matrix is lower. It is felt that this structure might be from a particle deficient region similar to that shown in Fig. 7c; hence it is probably not representative of the general deformation structure.

Although the strengthening phase promotes significant changes in the dislocation structure in the matrix, the NiAl–TiB_2 interface has remained intact, and no reaction layer could be seen between these two phases (Figs 10b, 10c and 10d). In many cases each particle appeared to be surrounded with a high density of loops (Fig. 10b) in addition to the usual misfit dislocations; however little dislocation activity could be found within the TiB_2 itself.

4. Discussion

The microstructural and mechanical property data clearly indicate that TiB_2 is a good choice for a strengthening phase in NiAl. The matrix–particle interface is maintained both during processing (Figs 1 and 2) and elevated temperature deformation (Figs 7, 8 and 10), the TiB_2 particles have been shown [13] to be unaffected by a 1 h heat treatment at 1773 K and, most importantly, the presence of the particulate leads to increased strength (Figs 3 to 6).

Examination of the structure of deformed composites (Fig. 10) indicates that there is little evidence of dislocation activity in the TiB_2 particles while considerable numbers of dislocations have been generated and moved through the NiAl matrix. These results are in agreement with other observations where, for example, Ramberg and Williams [14] did not witness plastic deformation in TiB_2 until the temperature exceeded ~ 1975 K, and Yang and Dodd [6] demonstrated the formation of subgrain boundaries in NiAl. Hence description of the elevated temperature behaviour of the NiAl–TiB_2 composites as hard, elastic particles in a soft, plastic matrix [19] seems to be appropriate.

Based on TEM photomicrographs from this study and the literature [4, 6, 8] elevated temperature deformation in NiAl is dislocation climb controlled with relatively dislocation-free subgrains as the characteristic microstructural feature. With the addition of a small fraction of second phases to NiAl, subgrains are still formed, but they can becomes attached to the particles (Figs 2a and 10c). Increases in the level of TiB_2 seems to further encourage the formation of subgrains between particles and significantly raises the dislocation density in the matrix (Figs 2b, 10b and 10d). Thus the microstructural evidence indicates that strength of the composites is due to a subgrain forming, dislocation climb mechanism in combination with the "cold work" like dislocation density.

The Sherby, Klundt and Miller [20] model of dislocation climb controlled creep indicates that stabilizing a small subgrain size can affect the deformation rate

$$\dot{\varepsilon} \propto (\lambda/b)^3(\sigma/E)^8 D_{eff} \qquad (5)$$

where λ is the subgrain size, b the magnitude of the Burgers vector, E the dynamic Youngs modulus, and D_{eff} an effective diffusion coefficient which is equal to the bulk diffusion coefficient for high temperature deformation conditions. For most subgrain forming materials Equation 5 is not obeyed in an obvious manner because the equilibrium subgrain diameter is inversely dependent on the applied stress as shown by Raj and Pharr [21]

$$\lambda = 23b(G/\sigma) \approx 8.8b(E/\sigma) \qquad (6)$$

where G is the shear modulus. Therefore the commonly found stress exponent is about 5, and this is the case for NiAl (see [6, 8] and Table II).

If the inverse relationship between applied stress and subgrain size could be circumvented, and a smaller diameter, but stable subgrain population maintained during deformation, increased strength in combination with an increase in the stress exponent, but unchanged activation energy should be found. Such behaviour has already been reported in small grain size NiAl [9, 10] for deformation conditions where the actual

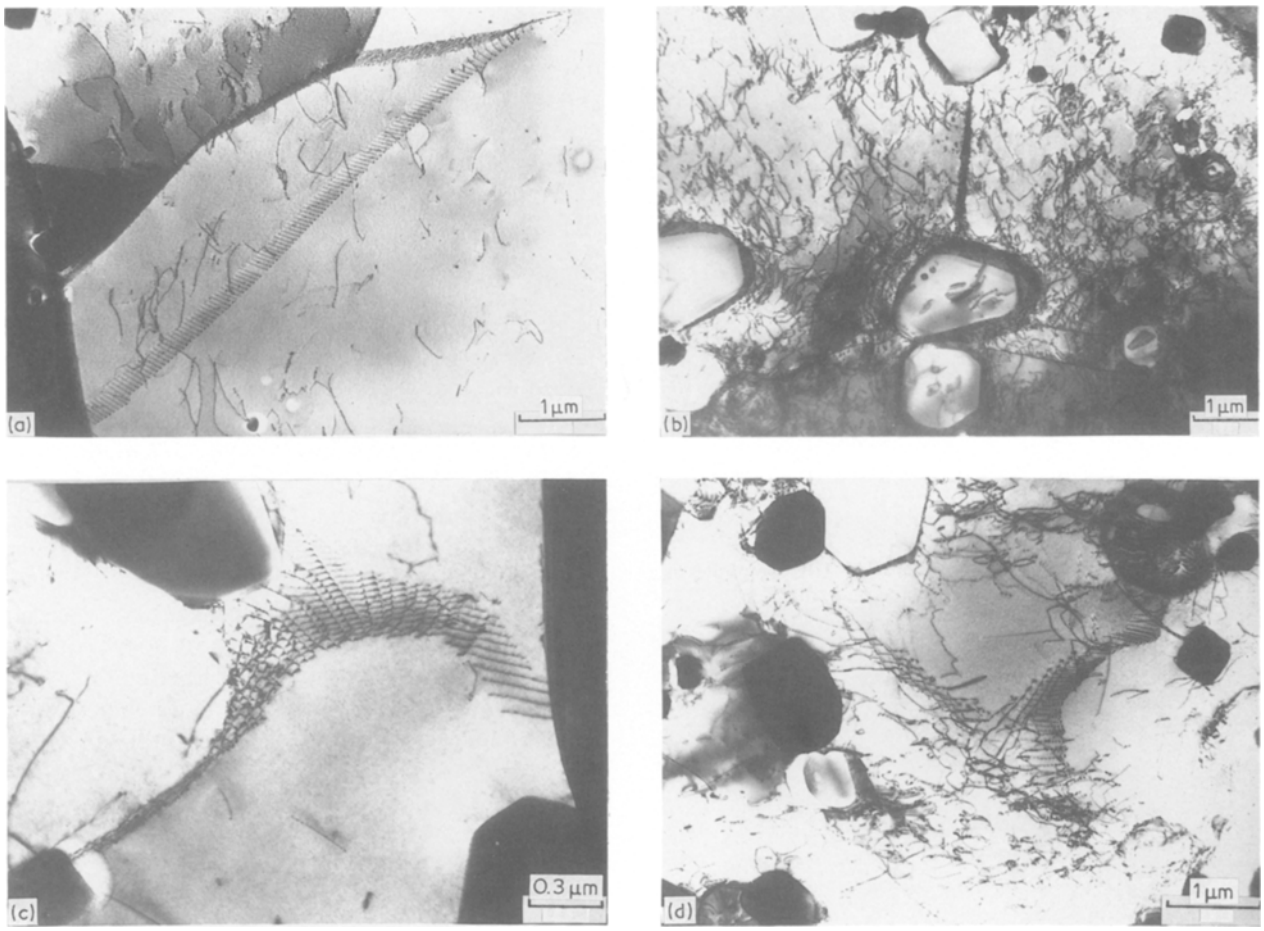

Figure 10 TEM photomicrographs of NiAl–TiB_2 composites after testing at 1300 K and $\sim 2. \times 10^{-7}$ sec^{-1}.

	Volume fraction (%)	Flow stress (MPa)	Approximate strain rate, sec^{-1}	Strain (%)
(a)	0	19.6	2×10^{-7}	9.4
(b)	10	53.2	2×10^{-7}	9.3
(c)	2.5	53.2	2×10^{-5}	13.6
(d)	20	147.2	2×10^{-4}	11.1

grain diameter was less than the subgrain size predicted from Equation 6. Therefore strengthening of NiAl–TiB_2 composites by subgrain refinement is quite possible as the particles can serve as pinning points (Figs 2 and 10) for a stable, small, non-equilibrium substructure.

While a subgrain refinement model can account for a portion of the increased strength of the composites, its role could be minor because the observed dependency on volume fraction (Equation 4) is not in agreement with Equation 5. If the composites contained a uniform distribution of identical spherical particles of radius r, the centre-to-centre particle spacing l would be given by

$$l = 1.61r/v^{1/3} \quad (7)$$

Since the approximate diameter of the particle stabilized subgrains in the TiB_2 composites should be about 1, Equation 7 can be substituted into Equation 5 for λ yielding

$$\dot{\varepsilon} \propto (r/b)^3(1/v)(\sigma/E)^8 D_{\text{eff}} \quad (8)$$

Thus for a material whose strength is entirely due to a particle stabilized subgrain size, this equation states that the strain rate should be inversely dependent on the particulate volume fraction. Clearly on the basis of the present experiments (Equation 4), this is not the case.

Subgrain deformation mechanisms are unable to completely account for the increased strength of the NiAl–TiB_2 composites; thus the second microstructural finding of a high dislocation density within the matrix must exert an influence on the deformation resistance of these materials. Most certainly cold work increases the strength of alloys; however such advantages are generally lost at elevated temperatures due to recovery. This might not be the case in particulate strengthened materials where the particles could affect recovery events. During high temperature slow plastic straining recovery would probably consist of a combination of dislocation glide, climb and cross slip steps. If any of these processes were inhibited, then recovery would be slowed and a high density, stronger dislocation structure maintained.

On the basis of activation energy data in Table IIb and Equation 4, it does not appear that the TiB_2 greatly affects thermal processes in the NiAl matrix; hence it is possible that the particles are not significantly

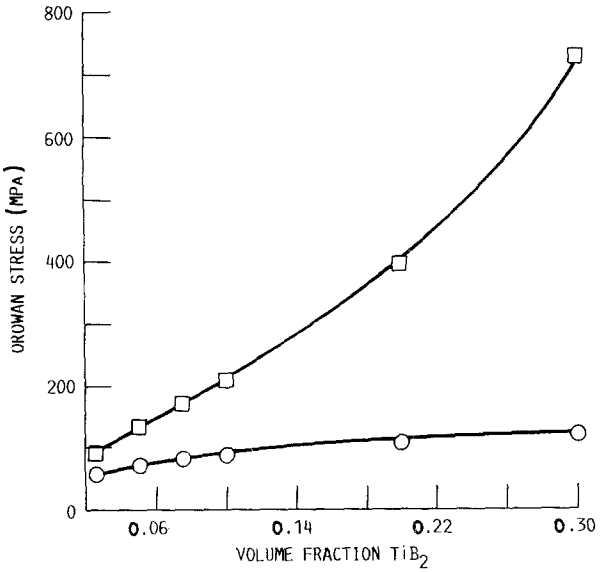

Figure 11 Estimated Orowan stresses in NiAl–TiB_2 composites as a function of volume fraction of TiB_2 particles.
□ $\sigma_{OR} \propto Gb/(l - d) \ln (d/b)$, O $\sigma_{OR} \propto Gb/l \ln (d/b)$.

reducing dislocation climb. However, the particles can influence dislocation glide due to the Orowan stress σ_{OR} necessary for dislocation bypass around the TiB_2. While there are many equations [22, 23] for the Orowan stress, most are of the form

$$\sigma_{OR} = C(Gb/l) \ln (2r/b) \quad (9)$$

where C is a geometric constant on the order of 1, and l is either the centre-to-centre interparticle distance, or it is replaced [23] by intraparticle spacing $l' = (l - 2r)$.

From the NiAl modulus data of Harmouche and Wolfenden [24] and the assumption of a uniform distribution of 1 μm diameter TiB_2 particles, the Orowan stresses can be estimated for the composites, and these σ_{OR} are shown in Fig. 11 as a function of TiB_2 volume fraction. While the estimated Orowam stresses vary with the model utilized, clearly the values are high and are comparable with the deformation resistance of these materials (Fig. 6). Thus disruption of normal dislocation glide is likely in the NiAl–TiB_2 composites, and recovery becomes inhibited which leads to strengthening of these materials.

Finally because dislocation mechanisms are temperature–time dependent, we wondered if it might be possible to deform unstrengthened NiAl under conditions which would produce structures similar to those found in the NiAl–TiB_2 composites. According to Raj [25] power law creep Equations 1 and 2 break down when

$$\sigma/G \geqslant 5 \times 10^{-4} \quad (10)$$

where G is the dynamic shear modulus. Based on the Youngs modulus data for NiAl [24], this criterion is met at 1300 K when the flow stress for NiAl exceeds 35 MPa. Comparison of this value with the stress–strain rate data in Fig. 6b indicates that power law creep would not be applicable for $\dot{\varepsilon} > 10^{-4}\,sec^{-1}$; therefore fast strain rate testing at 1300 K should form complex dislocation structures in NiAl.

To determine if NiAl could be deformed at 1300 K

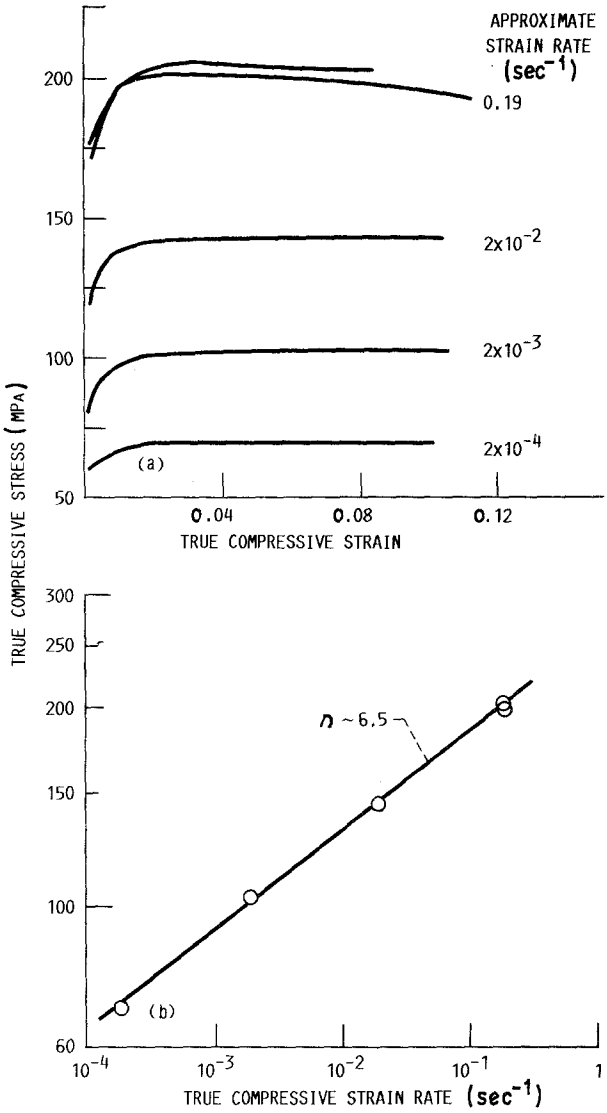

Figure 12 True compressive stress–strain diagrams (a) and true compressive stress–strain rate behaviour (b) for unreinforced NiAl tested at 1300 K and relatively fast cross-head speeds.

without just forming simple subgrains, compression tests were conducted at strain rates ranging from ~0.2 to $2 \times 10^{-4}\,sec^{-1}$. Although the stress–strain curves (Fig. 12a) show a transition from constant flow ($\dot{\varepsilon} \approx 2 \times 10^{-4}\,sec^{-1}$) to a diffuse yielding followed by strain softening ($\dot{\varepsilon} \approx 0.2\,sec^{-1}$) behaviour, the stress–strain rate data in Fig. 12b indicate that a power law description is still adequate (Table IIa). Moreover linear regression fitting of both the fast and slow test data in Table IIa indicate that a single stress exponent can precisely portray deformation in NiAl at 1300 K at strain rates ranging from 0.2 to $2 \times 10^{-7}\,sec^{-1}$.

Based on retention of power law behaviour and a stress exponent of about 6, it was expected that the microstructure of NiAl tested at the faster velocities would still be comprised of subgrains. As can be seen in Fig. 13, this is the case even though the measured flow stress is approximately six times Raj's estimate [25] for power law breakdown. Clearly the development and retention of a non-subgrain structure in NiAl will require much faster strain rates or, more realistically, lower test temperatures.

While the strength of the NiAl–TiB_2 materials is greater than the matrix, the oxidation resistance of

Figure 13 TEM microstructure of unreinforced NiAl tested at 1300 K and $\dot{\varepsilon} \approx 0.2\,\text{sec}^{-1}$ to 0.084 strain.

these composites is less than the unstrengthened aluminide as wider aluminium-deficient regions and multiphase structures can be formed (Table III and Fig. 9). The lower oxidation resistance of the composites is probably the result of decomposition of the TiB_2 via

$$TiB_2 = Ti + 2B \quad (11)$$

or

$$2TiB_2 + 5O_2 = 2TiO_2 + 2B_2O_3 \quad (12)$$

Based on the microstructural evidence (Fig. 9b) and microprobe results, dissociation according to Equation 11 followed by fast interstitial diffusion of boron to the matrix–oxide interface and its subsequent loss to the atmosphere seems to be the most likely sequence. Reaction 12 is not as probable since substitution diffusion of oxygen through intermediate layers (and nickel solid solution) would be slow, and little sign of the existence of TiO_2 particles in these layers can be found. In any case the successful use of NiAl–TiB_2 materials at elevated temperature requires that alloying studies for oxidation resistance in the matrix of the composite be undertaken; in particular reactive metal additions, such as zirconium which have been shown to promote the oxidation resistance in NiAl [26], should be investigated.

5. Conclusions

Based on a study of the elevated temperature slow plastic compressive behaviour of particulate NiAl–TiB_2 composites, it is concluded that the particles greatly influence the deformation mechanism(s). In particular the increased strength of the composites is due to a high dislocation density structure in possible combination with a reduced subgrain size whereas the creep resistance of the unreinforced matrix is due to maintenance of an equilibrium subgrain size. The stability of a high dislocation density in the composites is probably the result of reduced recovery from the inhibition of dislocation glide by the TiB_2 particles.

Acknowledgement

Three of us (RKV, SKM and BS) would like to acknowledge the funding support for this program by ONR under Contract N0014-85-C-0639, and JDW greatly appreciates the encouragement and provision of test facilities of the NASA-Lewis Research Center.

References

1. E. M. GRALA, in "Mechanical Properties of Intermetallic Compounds", edited by J. H. Westbrook (Wiley, New York, 1960) pp. 358–404.
2. A. G. ROZNER and R. J. WASILEWSKI, *J. Inst. Met.* **94** (1966) 169–175.
3. A. BALL and R. E. SMALLMAN, *Acta Metall.* **14** (1966) 1349–1355.
4. R. R. VANDERVOORT, A. K. MUKHERJEE and J. E. DORN, *Trans. ASM* **59** (1966) 930–944.
5. L. A. HOCKING, P. R. STRUTT and R. D. DODD, *J. Inst. Met.* **99** (1971) 98–101.
6. W. J. YANG and R. A. DODD, *Met. Sci. J.* **7** (1973) 41–47.
7. J. D. WHITTENBERGER, *Mater. Sci. Engng* **57** (1983) 77–85.
8. *Idem, J. Mater. Sci.* **22** (1987) 394–402.
9. *Idem, ibid.* **23** (1987) 235–240.
10. *Idem*, NASA, TM 101382 (1988).
11. K. VEDULA, V. PATHARE, I. ASLANIDIS and R. H. TITRAN, in "High-Temperature Ordered Intermetallic Alloys", edited by C. C. Koch, C. T. Liu and N. S. Stoloff, (Materials Research Society, Pittsburgh, PA, 1984) pp. 411–21.
12. M. SHERMAN and K. VEDULA, *J. Mater. Sci.* **21** (1986) 1974–1980.
13. R. K. VISWANADHAM, S. K. MANNAN and B. SPRISSLER, "Nickel Aluminide/Titanium Diboride Composites" Martin Marietta Laboratories TR 87-66c, 1987.
14. J. R. RAMBERG and W. S. WILLIAMS, *J. Mater. Sci.* **22** (1987) 1815–1826.
15. D. BROUSSAUD, H. PASTOR, R. MEYER and A. ACCARY, in "Modern Developments in Powder Metallurgy", edited by H. H. Hausner and W. E. Smith, (Metal Powder Industries Federation & American Powder Metallurgy Institute, Princeton, NJ, 1974) pp. 589–603.
16. J. D. WHITTENBERGER, *Mater. Sci. Engng* **73** (1985) 87–96.
17. R. W. CLARK and J. D. WHITTENBERGER, "Thermal Expansion 8", edited by T. A. Hahn (Plenum Press, New York, 1984) pp. 189–96.
18. High Temperature Materials – Mechanical, Electronic and Thermophysical Properties Information Analysis Center, Purdue University, West Lafayette, IN 47906.
19. L. M. BROWN, in "Fatigue and Creep of Composite Materials", edited by H. Lilholt and R. Talreja, (Riso National Laboratory, Roskilde, Denmark, 1982) pp. 1–18.
20. O. D. SHERBY, R. H. KLUNDT and A. K. MILLER, *Met. Trans* **8A** (1977) 843–850.
21. S. V. RAJ and G. M. PHARR, *Mater. Sci. Engng* **81** (1986) 217–237.
22. D. L. BACON, U. F. KOCKS and R. O. SCATTERGOOD, *Phil. Mag.* **28** (1973) 1241–1263.
23. R. W. LUND and W. D. NIX, *Acta Metall.* **24** (1976) 469–481.
24. M. R. HARMOUCHE and A. WOLFENDEN, *J. Test. Eval.* **15** (1987) 101–104.
25. S. V. RAJ, *Scripta Metall.* **20** (1986) 1333–1338.
26. C. A. BARRETT, "The Effect of 0.1 Atomic Percent Zirconium on the Cyclic Oxidation Resistance of β-NiAl", submitted to Ox. of Metals.

Received 22 September 1988
and accepted 24 February 1989